Determining Amplitudes of Standing Surface Acoustic Waves via Atomic Force Microscopy

Jan Hellemann,[1] Filipp Müller,[1] Madeleine Msall[1,2] Paulo V. Santos,[1] and Stefan Ludwig[1,*]

[1]*Paul-Drude-Institut für Festkörperelektronik, Leibniz-Institut im Forschungsverbund Berlin e.V., Hausvogteiplatz 5-7, Berlin 10117, Germany*
[2]*Bowdoin College, 255 Maine Street, Brunswick, Maine 04011, USA*

Atomic force microscopy is a tool for characterizing surface acoustic waves, in particular for high frequencies, where the wavelength is too short to be resolved by laser interferometry. A caveat is, that the cantilever deflection is not equal to the amplitude of the surface acoustic wave. We show that the energy transfer from the moving surface to the cantilever instead leads to a deflection exceeding the surface modulation. We present a method for an accurate determination of surface acoustic wave amplitudes based on comparing force-curve measurements with the equation of motion of a driven cantilever. We demonstrate our method for a standing surface acoustic wave on a GaAs crystal confined in a focusing cavity with a resonance frequency near 3 GHz.

I. INTRODUCTION

Today, surface acoustic waves (SAWs) are used in key technologies, for instance, as miniature radio-frequency filters in communication devices [1,2], for sensor applications [3,4], or for microcontrol of fluids on surfaces [5,6]. Commonly, SAWs are generated, detected, and controlled by employing interdigital transducers, periodic arrays of metallic finger gates with a pitch of half the SAW wavelength λ. Based on the piezoelectric effect, they convert resonant electrical signals into SAWs and vice versa and also function as Bragg mirrors for SAWs. Recent research aims at integrating SAWs into quantum technology [7], where high-quality phonon cavities that can harbor standing surface acoustic waves (SSAWs) at submicrometer wavelength are called for [8,9]. The cavity spectrum can be explored using the electric response of interdigital transducers [8]. More information, including amplitude and geometry of a SAW can be acquired by laser interferometry [10]. Unfortunately, for $\lambda/2 < 0.5$ μm the spatial resolution of laser interferometry becomes insufficient [10], while electric response measurements of SAWs become increasingly difficult and inaccurate at the corresponding high frequencies. Nevertheless, the ability to fully characterize high-frequency SAW devices would help improving radio-frequency filters for alternative technologies [2]. In particular, for optimizing phonon cavities for quantum applications, knowledge about the local distribution of the absolute amplitude of the SSAW modes as a function of

excitation power as well as their frequency dependence, would be extremely helpful [9].

An alternative method well suited for imaging SAWs with submicron wavelengths is atomic force microscopy [11], with one caveat: the cantilever deflection is not a direct measurement of a SAW amplitude. The reason is the low mechanical resonance frequency of less than 1 MHz of commonly used cantilevers, which cannot time resolve SAWs with much larger frequencies. In this case, a cantilever interacting with a SAW can be treated as a slow oscillator driven by an external periodic force modulated with a large frequency. The transfer of kinetic energy from the quickly moving surface into the cantilever then results in an elevated average position of the cantilever tip. As a result, the measured deflection of the cantilever overestimates the SAW amplitude, independent of the particular atomic force microscope (AFM) configuration. Here, we introduce a method to nevertheless calibrate the amplitude of a SSAW using a fixed-point analysis of AFM force-curve measurements.

In Fig. 1, we present an extraction of an AFM measurement of a GaAs surface including a SSAW with a period of $\lambda/2 = 500$ nm at a resonance frequency near $f = 3$ GHz. Clearly, the AFM measurement directly provides spatial information of a SSAW including the mode geometry and phase, which are useful for optimizing a cavity. Detecting, in addition, the frequency dependence as shown in Fig. 2(a), provides the mode spectrum of the SSAW cavity and the quality factor, here $Q \simeq 1100$. Thereby, the stop bands of the cavity-defining Bragg mirrors provide the overall frequency range in which cavity modes can
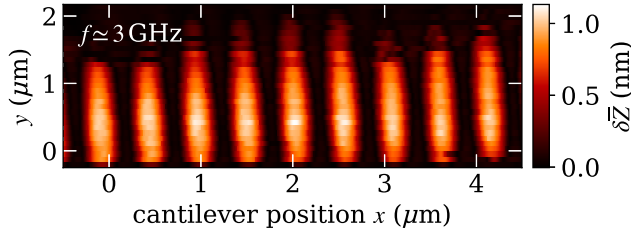
*ludwig@pdi-berlin.de

FIG. 1.   Two-dimensional AFM contact mode lock-in measurement of a SSAW with frequency $f \simeq 3$ GHz inside a focusing cavity on a GaAs surface using a sharp nitride cantilever with an eigenfrequency of $\omega/2\pi = 65$ kHz and a force constant of 0.32 N/m. The excitation power is sine modulated with the lock-in frequency of 250 Hz between $0 \le P \le 9$ dBm (P is the on-chip power after subtraction of cable losses, reflections, etc.). The color scale depicts the time-averaged difference $\delta\overline{Z}$ of the cantilever deflection with SSAW versus without SSAW. The propagation is in the [110] crystal direction along x.

develop. The AFM measurement presented in Fig. 2(a) includes four modes. For adjacent modes, the position of nodes and anti-nodes along the cavity is exchanged as expected at the center of the cavity [cf. dashed vertical line in Fig. 2(a)]. The mode separation is $\delta f = 12.5$ MHz corresponding to an effective cavity length of $\lambda f / 2\delta f \simeq 113$ μm. In Fig. 2(b), we show a segment of a SSAW
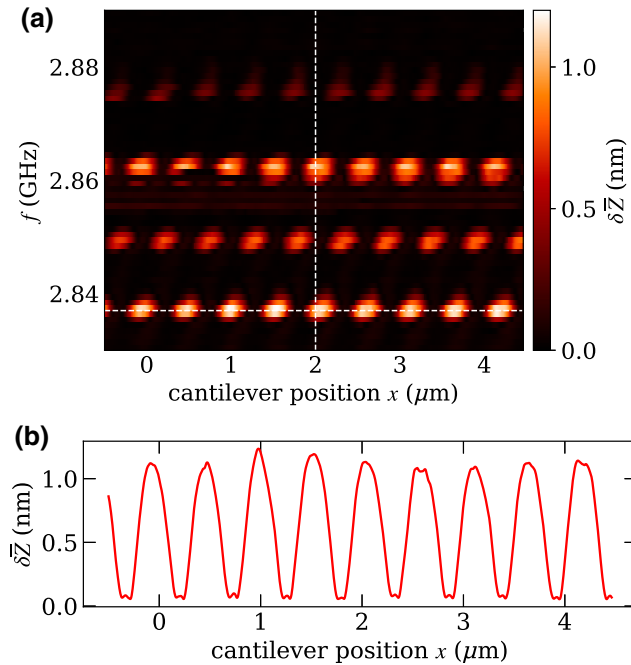

FIG. 2.   (a) AFM lock-in measurement showing $\delta\overline{Z}(x, f)$, details and parameters as explained in the caption of Fig. 1. The frequency range covers four cavity modes. The vertical line is a guide for the eye, revealing phase reversal between adjacent modes. (b) Individual line scan $\delta\overline{Z}(x)$ along the horizontal line in (a) at $f = 2.837$ GHz.

along the horizontal dashed line in Fig. 2(a). It indicates that the cantilever deflection oscillates by $\gtrsim 1$ nm between nodes and antinodes of this SSAW mode powered with $P = 9$ dBm.

II. SETUP AND MEASUREMENTS

In Fig. 3, we present a scanning electron micrograph of the surface of our sample. It displays metal gates in dark gray on the (001) surface of a GaAs wafer shown in light gray. The enlargement reveals fingers of a Bragg mirror with a pitch of 500 nm for SAWs. The sample contains two matching Bragg mirrors, which together define a cavity for surface phonons in the 100 μm opening between them. While one of the Bragg mirrors is grounded, every second finger of the other Bragg mirror is connected to a radio-frequency source. This way it serves as an interdigital transducer to generate a SAW. The arched fingers of the mirrors are optimized to reflect a resonant SAW such that a focused standing wave emerges inside the cavity [10].

For recording the surface scans shown in Figs. 1 and 2 we employ the atomic force microscope *Edge* by Bruker in contact mode at a constant force. However, to determine the actual SSAW amplitude, we perform force curves: after moving the tip of the AFM cantilever to the position of an antinode of the SSAW we measure the cantilever deflection, while vertically approaching the cantilever first towards and pushing it against the surface and then retracting it. Such a vertical motion can be accurately controlled and monitored in an AFM using a piezoelectric motor. In Fig. 4, we present force-curve measurements for two different SSAW powers. Plotted is the time-averaged deflection $\overline{Z}$ of the cantilever (averaged over the resonant cantilever oscillations and many SSAW periods) as a function of its preset vertical position z_0, which is changed at a rate much slower than the surface modulation by the SSAW. The position z_0 is the distance that the tip would have from the surface if the cantilever were not deflected [cf. Fig. 6]. The dashed line is measured during the approach of the cantilever and the solid line while retracting it from the surface. As long as the cantilever moves freely above
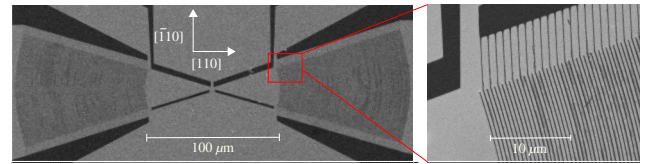

FIG. 3.   Scanning electron micrograph of the (001) surface (light gray) of a GaAs wafer partly covered with (10 nm/30 nm/10 nm Ti/Al/Ti) metal gates (dark gray). The enlargement reveals the 250-nm-wide metal fingers at a pitch of 500 nm forming a Bragg mirror. Two such Bragg mirrors define within the 100-μm-long spacing between them a surface phonon cavity oriented along the [110] crystal direction.
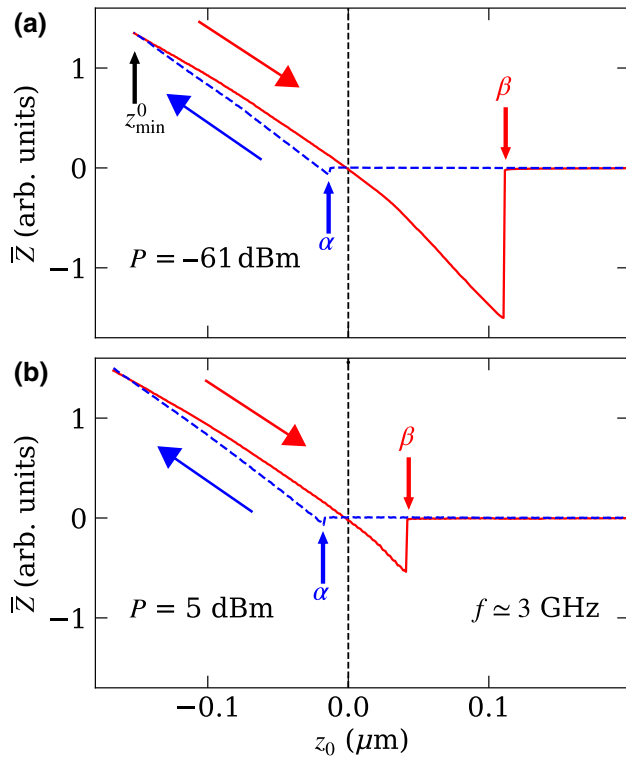
FIG. 4.   Force curves recorded for an antinode of a SSAW near 3 GHz for two different SSAW powers, $P = -61$ dBm in (a) and 5 dBm in (b). Plotted is the time-averaged cantilever deflection $\overline{Z}$ as a function of the preset cantilever position z_0, explained in the text. The dashed lines are measured during the approaches of the cantilever towards the surface whereas the solid lines correspond to the subsequent retractions. The position where the cantilever starts to touch the surface is indicated as α and the point of detachment as β. The latter strongly depends on P.

FIG. 5.   Position of detachment of the cantilever, $z_0 = \beta$, as a function of the SSAW power P for various points of return z_0^{min}, cf. Fig. 4. For $z_0^{min} \gtrsim -150$ nm the curves $\beta(P)$ are independent of z_0^{min}. The cantilever tip is positioned at an antinode of a SSAW mode near 3 GHz.

the surface its deflection remains zero during approach. A small kink of negative deflection at $z_0 = \alpha$ points to an attractive force, which pulls the cantilever tip to the surface. As we continue to move the cantilever forward, the hard surface pushes its tip backwards, such that we measure an approximately linearly increasing positive deflection. The (almost) constant slope can be used for a rough calibration of the vertical AFM tip position.

During the subsequent retraction of the cantilever (solid line) the slope of the force curve is slightly smaller but increases with z_0, giving rise to a negative curvature. The hysteresis between the approach versus retraction curves in the region of positive deflection and $z_0 < 0$ is reproducible and commonly observed. It is interpreted in terms of a radial shirk of the cantilever [12]. Unfortunately, it conceals the accurate potential between tip and surface. For practical reasons, we define $z_0 = 0$ at zero average deflection of the cantilever during retraction, $\overline{Z} = 0$. It coincides with the crossing between the retraction curve and the still horizontal approach curve. Note, that in the limit of large z_0 the deflection of the cantilever also vanishes.
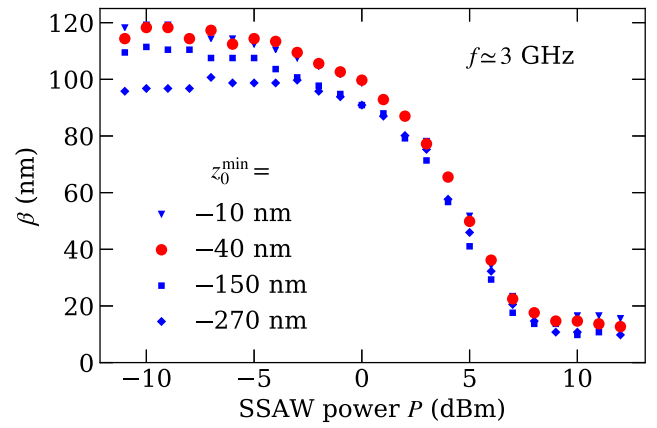
While the cantilever is further retracted for $z_0 > 0$, for the time being its tip stays connected to the surface, such that $\overline{Z} < 0$ because of the attractive force between the surface and the tip. Finally, at a height of $z_0 = \beta$ the spring force of the cantilever surpasses the attraction force and the cantilever flips back to stall at $\overline{Z} = 0$. The resulting deflection curve is characterized by a sizable triangle at negative deflection, which marks a peculiar hysteresis between approach and retraction for $z_0 > 0$. This triangular hysteresis indicates a competition between two stable solutions.

In Fig. 4(a) the SSAW power of $P = -61$ dBm applied to the interdigital transducer is so small that no SSAW can be detected with the AFM, and the force-curve resembles that of an unperturbed surface. In Fig. 4(b), we show the same measurement but with the cantilever tip being positioned at the antinode of a relatively strong SSAW at the frequency near $f = 3$ GHz. Strikingly, the strong SSAW causes the hysteresis between approach and retraction curves, quantified as β, to be reduced. In Fig. 5 we summarize the result of many measurements by presenting $\beta(P)$. Clearly, an increase of the SSAW power causes a smaller β. The physical reason is a reduction of the attractive force, between the cantilever tip and the surface as the cantilever tip is pushed further away by a stronger surface modulation.

For practical purposes, throughout the paper we state the SSAW power P estimated from the power actually applied at the generator reduced by cable losses and the electroacoustic coupling. For the large Q factor of our cavity we can neglect internal losses and estimate the SSAW power from comparing the applied electrical signal with that transmitted through the cavity. Our analysis suggests a reduction of $\simeq 11$ dB compared to the generated radio-frequency signal. Note, that this estimate of the SSAW
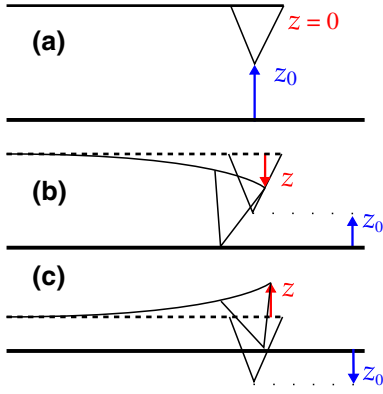
FIG. 6. Sketch of the experiment illustrating various characteristic cantilever positions for $R = 0$ (no SSAW). The deflection of the cantilever is z, the distance between surface and the tip at $z = 0$ is z_0. (a) A free cantilever $z = 0$ and $z_0 > 0$, (b) a cantilever pulled towards the surface with $-z > z_0 > 0$, (c) a cantilever bent away from the surface with $-z \simeq z_0 < 0$.

power by measuring the electrical transmission becomes more and more difficult and inaccurate with increasing frequency. Here P serves as a reference, but its actual value is not needed to determine the amplitude R of the SSAW, see below.

A conversion of the SSAW power P to its amplitude R requires the knowledge of the function $R(P)$. While $P \propto R^2$ is evident for small powers, the proportionality factor is *a priori* unknown and depends on material parameters and the exact knowledge of the power reduction factor discussed above. Our model below offers an alternative for the determination of the SSAW amplitude R without requiring knowledge of either the power reduction factor or the proportionality factor. However, our model assumes the validity of $P \propto R^2$, which can be controlled in experiment and is the case for small enough amplitudes.

III. MODEL AND ANALYSIS

For a quantitative analysis of the measured $\beta(P)$ and to determine the SSAW amplitudes, we introduce a model describing the dynamics of the cantilever interacting with the surface modulated by a SSAW.

The equation of motion (EOM) of the cantilever can be derived from Newton's third law, $-F_{cl} = F_i$, where F_{cl} is the cantilever spring force and F_i the interaction force between the tip of the cantilever and the surface. It can be written as

$$m\left(\ddot{z} + \omega^2 z\right) = -V'\left[z + z_0 + R\cos(\Omega t)\right]. \quad (1)$$

Here, $z(t)$ denotes the momentary cantilever deflection and V the interaction potential with $F_i = -V' = -\partial V/\partial z$. The cantilever is characterized by its force constant and its resonance frequency, we have $m\omega^2 \simeq 0.32$ N/m

and $\omega/2\pi \simeq 65$ kHz, respectively (manufacturer specifications). The momentary distance between the tip and the surface is $z + z_0 + R\cos(\Omega t)$. The last term thereby describes the modulation of the surface by the SSAW with amplitude R and frequency $f = \Omega/2\pi$. In Figs. 6(a) and 6(c), we sketch the cantilever setup and indicate z and z_0 for three relevant situations. Table III in Appendix A provides a summary of the definitions of variables with units of length.

As long as the frequency of the SSAW is orders of magnitude larger than the resonance frequency of the cantilever, in our case $\Omega/\omega > 10^4$, we can separate the cantilever deflection into [13]

$$z(t) = Z(t) + \xi(t), \quad (2)$$

where $Z(t)$ moves slowly at a rate close to ω while $\xi(t)$ varies much faster at a rate near Ω. Because the cantilever is too slow to follow the motion of the SSAW we can assume $Z \gg \xi$. We also expect $Z \gg R$ as a consequence of the transfer of kinetic energy of a hard surface to a soft cantilever. Our experimental findings confirm the latter assumption *post priori*. A Taylor expansion of V' around $R = 0$ yields

$$V'\left[z + z_0 + R\cos(\Omega t)\right] \simeq V'(z + z_0)$$
$$+ V''(z + z_0)R\cos(\Omega t) + V'''(z + z_0)\frac{R^2}{2}\cos^2(\Omega t). \quad (3)$$

Expanding the potential derivatives on the right-hand-side of Eq. (3) around $\xi = 0$ while neglecting all terms $\propto \xi^2$ or beyond the third derivative of V we find

$$V'(z + z_0) \simeq V'(Y) + V''(Y)\xi,$$
$$V''(z + z_0) \simeq V''(Y) + V'''(Y)\xi,$$
$$V'''(z + z_0) \simeq V'''(Y), \quad (4)$$

where we introduce the slowly moving contribution of the cantilever tip distance from the surface $Y(t) = Z(t) + z_0$. Next, we split the EOM into one for the slowly varying $Z(t)$

$$m(\ddot{Z} + \omega^2 Z) \simeq -V'(Y) - V'''(Y)R\left[\overline{\xi\cos(\Omega t)} + \frac{R}{4}\right] \quad (5)$$

and another one for the fast oscillating $\xi(t)$

$$m(\ddot{\xi} + \omega^2\xi) \simeq -\left[V''(Y) + V'''(Y)R\cos(\Omega t)\right]\xi$$
$$- \left[V''(Y) + V'''(Y)\frac{R}{2}\cos(\Omega t)\right]R\cos(\Omega t). \quad (6)$$

Our goal is to establish a relation between the measured slowly varying contribution of the deflection of the cantilever, $Z(t) = Y(t) - z_0$, and the actual amplitude of the SSAW, R. From Eq. (6) we can directly calculate $\xi(t) \propto \cos(\Omega t)$ using $\ddot{\xi} = -\Omega^2 \xi$ while neglecting $\omega^2 \xi \ll \ddot{\xi}$ and insert $\xi(t)$ into Eq. (5). Further replacing $R\overline{\xi \cos(\Omega t)}$ in Eq. (5) by the leading term of its Taylor expansion around $R = 0$,

$$R\overline{\xi \cos(\Omega t)} = \frac{V''(\overline{Y})/2}{m\Omega^2 - V''(\overline{Y})} R^2 + \mathcal{O}(R^4), \qquad (7)$$

we finally predict the average steady-state cantilever deflection (neglecting $\overline{\bar{\xi}} \ll \overline{Z}$)

$$\overline{Z} = -\frac{V'(\overline{Y})}{m\omega^2} + \delta\overline{Z} \text{ with}$$

$$\delta\overline{Z} = -\frac{V'''(\overline{Y})}{4m\omega^2} \frac{m\Omega^2 - 3V''(\overline{Y})}{m\Omega^2 - V''(\overline{Y})} R^2. \qquad (8)$$

Here, we use $\ddot{Z} = 0$ in the steady state and introduce the average distance between the cantilever tip and the surface $\overline{Y} = \overline{Z} + z_0$ and the average steady-state contribution of the SSAW to the deflection $\delta\overline{Z} \propto R^2$. The solution, Eq. (8), is resilient for $R \leq 0.305$ Å, which is the convergence radius of the Taylor expansion leading to Eq. (7). It describes the steady-state balance of forces $-F_{cl} \equiv m\omega^2 \overline{Z} = -V'(\overline{Y}) + m\omega^2 \delta\overline{Z} \equiv F_i$.

The interaction potential V and the amplitude R of the SSAW are *a priori* unknown, albeit for $R = 0$ Eq. (8) provides a direct relation between $V'(\overline{Y})$ and the average deflection $\overline{Z}$. Unfortunately, the radial shirk of the cantilever while measuring the force curve [12] leads to a strong hysteresis (cf. Fig. 4 for $z_0 < 0$). This prevents us from determining the interaction potential with sufficient accuracy from force-curve measurements.

Nevertheless, from the force curve for $R = 0$ [cf. Fig. 4(a)], we can estimate the attraction between the tip and the surface at $z_0 = \beta = -\overline{Z}$ just before the cantilever detaches from the surface during retraction: $F_i(\beta) = -F_{cl}(\beta) = -m\omega^2 \beta \simeq -40$ nN, which points to interatomic forces holding the tip at the surface. A potential derived from interatomic forces acting between a single atom and a diamond structured semiconductor crystal was introduced by Tersoff for the case of Ge [14]. As a practical approach, we use the Tersoff potential but slightly vary its numerical values such that it fits our data measured on a (100)-GaAs surface. In detail, we increase the attractive contribution B by 1.9% and the cutoff parameter S_0 by 0.7%, while leaving all other parameters unchanged, see Appendix A. The modifications are small, as expected because of the similar lattices and densities of GaAs and Ge. For completeness, in Fig. 7, we illustrate the optimized Tersoff potential V and the corresponding interaction force $F_i = -V'$.
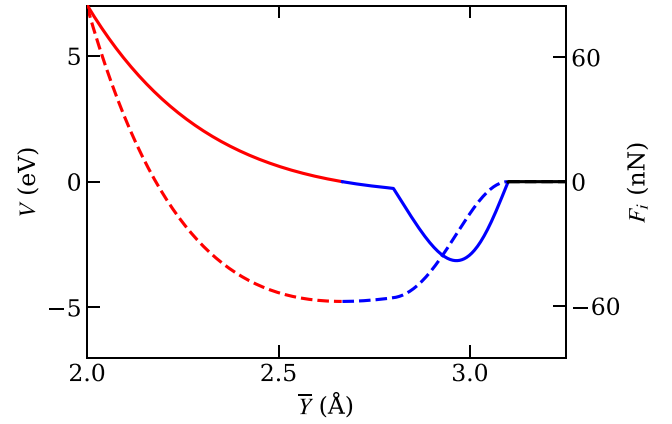

FIG. 7. Optimized Tersoff potential V (dashed line, left axis) and interaction force $F_i = -V'$ (solid line, right axis). Red color indicates regions of repulsive force $F_i > 0$ and blue regions attractive force $F_i < 0$. See Table II in Appendix A for parameters.

In Fig. 8 we sketch a series of snapshots for various values of z_0 during a force-curve measurement with $R = 0$. We plot the interaction force F_i (solid line) and the negative spring force of the cantilever $-F_{cl} = m\omega^2 Z = m\omega^2(Y - z_0)$ (dashed line) as a function of the distance Y between surface and cantilever tip. The upper panels (a)–(d) depict the approach and the lower ones (d)–(a) the retraction of the cantilever. Solutions of the EOM correspond to the intersection points $F_i = -F_{cl}$. Depending on z_0, up to three solutions coexist, two of which correspond to stable fixed points. The variations between the approach versus retraction curve in Fig. 4 for $z_0 > 0$ are related to switches between the two stable fixed points. In Fig. 8 the momentarily occupied fixed point is encircled. The fixed point labeled "I" corresponds to a stable solution with the cantilever tip far above the surface and $Y \simeq z_0$, while fixed point "II" is occupied, whenever the tip is in contact with the surface and Y is small (but $Z \simeq -z_0$).

Switches between stable fixed points happen at the transition from three coexisting solutions to a single solution, corresponding to the points of exactly two solutions. During the approach we observe a switch from fixed point "I" to "II" at $z_0 = \alpha$ [as indicated in Fig. 8(c)], where the attraction of the tip by the surface overcomes the cantilever spring force while $Y \simeq z_0$ and $Z \simeq 0$. During retraction, the switch back from "II" to "I" happens at $z_0 = \beta$ [as indicated in Fig. 8(f)] where the cantilever spring force overcomes the attraction while $Y \ll z_0$ and $Z \simeq -z_0$.

In order to fit our model to the measured data, we use the cantilever position $z_0 = \beta$ in Fig. 4 during retraction. Here, exactly two solutions exist, such that not only the forces are equal, $F_i = -F_{cl}$, but also their derivatives $-dF_{cl}/d\overline{Y} = dF_i/d\overline{Y}$, in short $-F'_{cl} = F'_i$, where $-F'_{cl} = m\omega^2 = 0.32$ N/m. In Fig. 9 we graphically visualize the two conditions by plotting $F_i(\overline{Y})$ while varying the SSAW
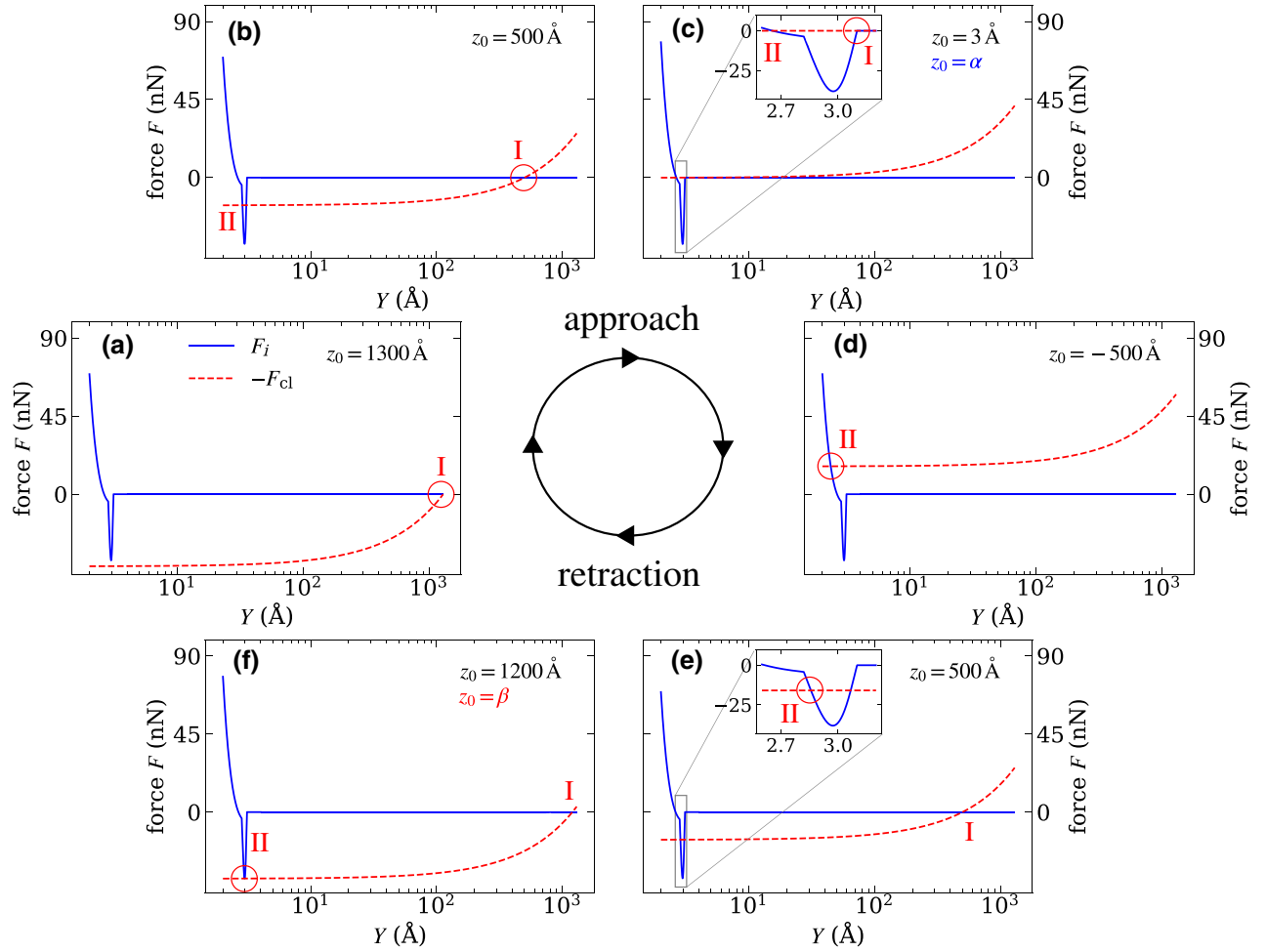
FIG. 8. Solutions of the EOM for various cantilever positions during approach [(a) → (d)] and retraction [(d) → (a)]. (a) Tip is far away from the surface, cantilever spring force $F_{cl} = 0$, fixed point I is the only solution; (b) tip is approached closer to the surface, three possible fixed points, while I is occupied; (c) as soon as $z_0 < \alpha$: transition between fixed points I → II; (d) tip is in contact with the surface, $z_0 < \alpha$, fixed point II is the only solution; (e) tip remains in contact with the surface during retraction, three fixed points exist, while II is occupied; (f) as soon as $z_0 > \beta$: transition between fixed points II → I.

amplitude within the convergence radius of our solution between $0 \le R \le 0.305$ Å. The black line, which connects the points with slope $F_i' = -F_{cl}'$, corresponds to the solution $\beta(R)$ with $\beta = \overline{Y} - \overline{Z} = \overline{Y} - F_i(\overline{Y})/m\omega^2$.

Comparing the range of $\overline{Y}$ in Fig. 9 with that of β in Fig. 5, we find that $\overline{Y} \ll \beta$, hence, $\overline{Z} \simeq -\beta$ for all our measurements. This is a direct consequence of the soft cantilever spring compared to a hard surface with the attraction force rapidly decaying with the distance Y between tip and surface. It is the reason for the triangular shape of the corresponding hysteresis in Fig. 4 and leads to the observation $\delta\overline{Z}(z_0 = \beta) \simeq \beta_{max} - \beta$, where $\beta_{max} = \beta(R = 0)$. We use the measurements of $\beta(P)$ for calibrating standard AFM measurements with $z_0 \ll \beta$.

Our model predicting $\delta\overline{Z} \propto R^2$ in Eq. (8) for arbitrary z_0 is limited to moderate powers, in particular where $R^2 \propto P$

is valid, too. To determine the proportionality factor $C = P/R^2$, we iteratively adjust both, the parameters of the Tersoff potential as well as C until we find the best overall fit within the range of validity of our model. In Fig. 10 we present the resulting calibration curve R as a function of $\sqrt{1 - \beta/\beta_{max}}$ (points) determined from the measured $\beta(p)$ (points in the inset). Two model curves based on optimized Tersoff potentials are shown as solid and dashed lines, respectively. The straight dotted line represents $R \propto \sqrt{\beta_{max} - \beta}$, which states that $(\beta_{max} - \beta) \propto P$ for small powers and $\beta \ll \beta_{max}$. The parameters used for the model curves and the accuracy of the result are discussed in Appendix A.

The shaded region in Fig. 10 indicates that for $R \gtrsim 0.2$ Å or $P \gtrsim 8$ dBm we begin to observe nonlinear effects in AFM measurements of the SSAW showing as a reduction of the measured deflection, power broadening of the
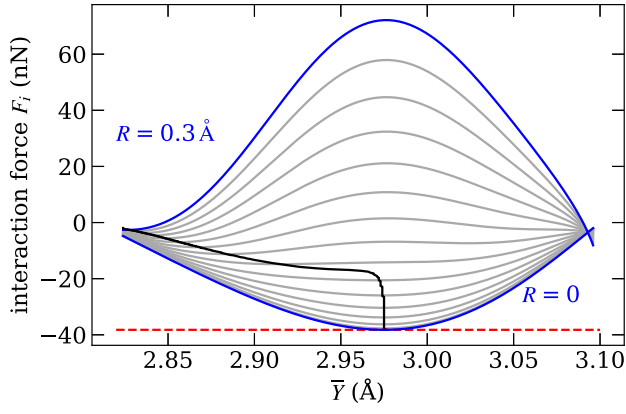
FIG. 9. Interaction force F_i as a function of the averaged tip-surface distance $\overline{Y}$ for various SSAW amplitudes $0 \leq R \leq 0.3$ Å as numerically determined by derivation of the optimized Tersoff potential shown in Fig. 7. The difference in R between two adjacent curves is 0.02 Å. The black line connects the points of $F_i(\overline{Y})$ with slopes of 0.32 N/m corresponding to the solutions at the cantilever detachment position β. The dashed red line is $F_{\mathrm{cl}}(\overline{Y})$ for $R = 0$.

SSAW antinodes and frequency shifts. At these large powers $P \propto R^2$ is no longer valid. However, for smaller powers, the overall agreement between our measured data and the model curve is excellent.

IV. CONCLUSIONS

In atomic force microscopy, one directly measures the deflection of the cantilever. For a SAW with a frequency exceeding the resonance frequency of the cantilever by
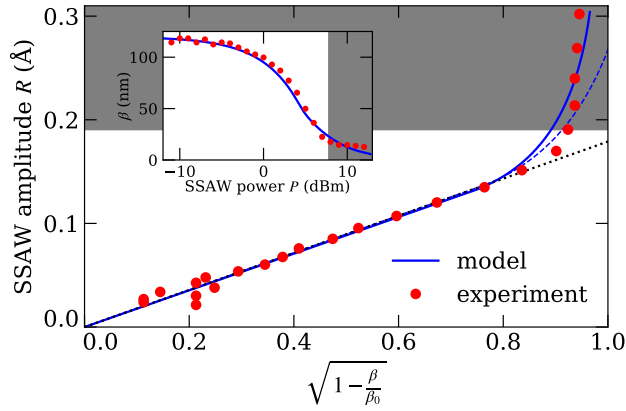

FIG. 10. SSAW amplitude R as a function of $\sqrt{1 - \beta/\beta_{\max}}$ determined for $z_0^{\min} = -40$ nm from the measured $\beta(P)$, shown in the inset and in Fig. 5. The cantilever tip is positioned at an antinode of a SSAW mode near 3 GHz. The solid and dashed lines are model predictions, see Table II in Appendix A for parameters. The solid line corresponds to the potential shown in Fig. 7. The straight dotted line has the form $R \propto \sqrt{\beta_{\max} - \beta}$. Within the shaded region measured points are uncertain due to nonlinear effects, cf. main text.

far, the measured deflection $\overline{Z}$ can be orders of magnitude larger than the actual amplitude R of the surface modulation. The steady-state solution of the EOM describes the cantilever deflection $\delta\overline{Z}(R)$ in response to the surface acoustic wave. The deflection thereby depends on the derivatives of the interaction potential V, which however is unknown. As a workaround, we iteratively fit a suggestive model potential to the measured relation between the SSAW power P and a characteristic length scale β of the experimental force curve, which marks a switch over between two stable solutions. In this way it is possible to reliably calibrate the actual amplitude R of a standing surface acoustic wave, and ultimately as a function of the measured cantilever deflection.

Based on force-curve measurements we successfully calibrate SSAW amplitudes within the limit of small powers with $R^2 \propto P$. The cantilever deflection in contact mode, cf. Fig. 2(b) for $P = 9$ dBm, is in our measurements 50 times larger than the actual SSAW amplitude.

APPENDIX: OPTIMIZED TERSOFF POTENTIAL

Tersoff derived empirical interatomic potentials for pure C, Si, and Ge crystals and also demonstrated that only tiny modifications of these potentials are necessary to describe multicomponent systems such as SiGe [14]. Here we start from the Tersoff potential for Ge and modify it to describe the interaction between a GaAs surface and a nitride cantilever tip. While the lattice parameters of Ge and GaAs are similar it is still surprising, how well this approach works.

The Tersoff potential is defined as [14]

$$V_{\mathrm{Ters}} = q f_C(Y)[A \exp(-\nu Y) - bB \exp(-\mu Y)], \quad (\mathrm{A1})$$

where

$$f_C(Y) = \begin{cases} 1, & Y < S_0 \\ \dfrac{1}{2} + \dfrac{1}{2}\cos\left[\pi \dfrac{Y - S_0}{S_1 - S_0}\right], & S_0 < Y < S_1 \\ 0, & Y > S_1 \end{cases}$$

and

$$b = [1 + \beta^n[f_C(Y)g(\theta)]^n]^{-1/2n}$$

with

$$g(\theta) = 1 + \frac{c^2}{d^2} - \frac{c^2}{d^2 + [h - \cos(\theta)]^2}.$$

TABLE I. Parameters of the Tersoff potential: original values for Ge [14], optional modification factors, corresponding scaling factors q and the coefficients of determination. Only one of the parameters is modified at a time to adopt the potential.

Parameter of Tersoff potential	Original value for Ge	Optional modification factor	Scaling factor q	Coefficient of determination (R^2 score)
A (eV)	1769	0.981	4.195	0.893
B (eV)	419	1.019	4.12	0.892
ν (Å^{-1})	2.4451	1.0032	4.175	0.906
μ (Å^{-1})	1.7047	0.995	4.065	0.913
β	9.0166×10^{-7}	0.914	4.205	0.947
n	0.756 27	1.04	4.165	0.923
c	106 430	0.955	4.2	0.949
d	15.652	1.025	4.2	0.957
h	−0.438 84	0.885	4.205	0.947
S_0 (Å)	2.8			
S_1 (Å)	3.1			
θ	$\pi/4$			
q	1			

The parameters originally derived for Ge [14] are listed in Table I. To fit our data measured with a sharp nitride cantilever on a GaAs surface it is sufficient to modify a small number of these parameters. To determine the interaction between the cantilever tip and the surface, the Tersoff potentials between the tip and all individual atoms on the surface have to be summed up. We reduce this three-dimensional problem to a one-dimensional calculation by reducing the tip to a single atom and making use of the symmetry of the (001)-GaAs surface. We account for the interaction between the tip centered between four surface atoms by multiplying the Tersoff potential in Eq. (A1)
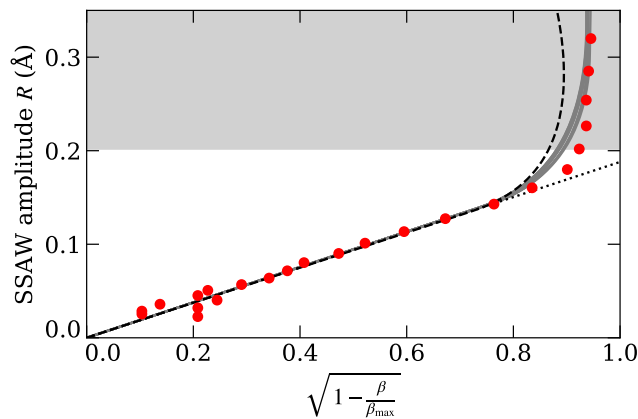

FIG. 11. Calibration data similar to those in Fig. 10 of the main paper (symbols) in comparison with the model predictions (gray lines), each for one variable modified according to Table I. The curve shown in dashed black corresponds to the unmodified Tersoff potential. The dotted curve is a straight line through the origin.

TABLE II. Parameters of the original Tersoff potential and their modifications for the model curves presented in Fig. 10 of the main paper. Only parameters, which we actually modify, are listed.

Parameter of Tersoff potential	Original value for Ge	Modified value used	Scaling factor q used	Coefficient of determination (R^2 score)
Solid lines in Figs. 10 and 7 of the main paper:				
B (eV)	419	427	3.9	0.968
S_0 (Å)	2.8	2.82	3.9	0.968
Dashed line in Fig. 10 of the main paper:				
B (eV)	419	440	3.635	0.979
S_0 (Å)	2.8	2.82	3.635	0.979

with a scaling factor $q \sim 4$. Within a self-consistent fitting procedure, we then optimize the values of q such that a single modified Tersoff potential reproduces the measured interaction force of $F_i = 40$ nN for $R = 0$. In the next step we optimize the factor $C = P/R^2$ and select parameters of the Tersoff potential to achieve the best possible agreement between the measured data $\beta(P)$ and the predicted curve $R(\beta)$.

To achieve a fair agreement, it is sufficient to slightly modify just one of the 12 parameters of the original Tersoff potential for Ge. In Fig. 11 we plot nine example model curves (gray lines) together with the experimental calibration data as in Fig. 10 of the main paper. The dashed black line is calculated from the original Tersoff potential for Ge. In Table I we list the optional modification factors, q, and the coefficient of determination (R^2 score). The conversion factor is $C = 123$ mW/Å^2. The variations between the gray lines are relatively small and occur mainly for high powers, where our model prediction stops being accurate. For $\beta \ll \beta_{\max}$, even the original Tersoff potential agrees well with our measurements.

TABLE III. Definitions of variables with units of length.

Variable	Explanation
z_0	Distance between tip and surface for zero deflection
$z(t) = Z(t) + \xi(t)$	Momentary deflection of cantilever
$Z(t)$	Slowly varying contribution of $z(t)$ (rate near ω)
$\xi(t) \ll Z(t)$	Quickly varying contribution of $z(t)$ (rate near Ω)
$Y(t) = Z(t) + z_0$	Distance between tip and surface (rate near ω)
$\overline{Z}$	Deflection of cantilever averaged over time
$\overline{Y} = \overline{Z} + z_0$	Averaged distance between tip and surface
$\delta\overline{Z} = \overline{Z} - \overline{Z}(R=0)$	Contribution of $\overline{Z}$ caused by SSAW
R	amplitude of SSAW

In the main paper we choose to vary B in conjunction with S_0 as a larger value of B corresponds to an increased binding energy. Qualitatively, this correction is supported by a larger melting point of GaAs at $T = 1511$ K compared to that of Ge at $T = 1211.4$ K. In Table II we summarize the modifications of the Tersoff potential, which yield the model lines in Fig. 10 of the main paper. The conversion factor is $C = 138$ mW/Å^2, which is roughly 10% larger than the one found above for varying one parameter less. This difference corresponds just about to the accuracy of a linear fit to our data for $\beta \ll \beta_{\text{max}}$ (dotted line), which yields the overall accuracy of our calibration result.

Finally, in Table III we list and explain the variables with units of length introduced in the main paper.

---

[1] C. C. W. Ruppel, Acoustic wave filter technology – a review, IEEE Trans. Ultrason. Ferroelectr. Freq. Control **64,** 1390 (2017).

[2] S. Mahon, The 5g effect on rf filter technologies, IEEE Trans. Semicond. Manuf. **30,** 494 (2017).

[3] V. Kalinin, in *2011 IEEE International Ultrasonics Symposium* (2011), p. 212.

[4] J. Devkota, P. R. Ohodnicki, and D. W. Greve, SAW sensors for chemical vapors and gases, Sensors **17,** 801 (2017).

[5] A. Wixforth, Acoustically driven programmable microfluidics for biological and chemical applications, JALA: J. Assoc. Lab. Automation **11,** 399 (2006).

[6] X. Ding, P. Li, S.-C. S. Lin, Z. S. Stratton, N. Nama, F. Guo, D. Slotcavage, X. Mao, J. Shi, F. Costanzo, and T. J. Huang, Surface acoustic wave microfluidics, Lab Chip **13,** 3626 (2013).

[7] P. Delsing, A. N. Cleland, M. J. Schuetz, J. Knörzer, G. Giedke, J. I. Cirac, K. Srinivasan, M. Wu, K. C. Balram, C. Bäuerle, and T. Meunier, The 2019 surface acoustic waves roadmap, J. Phys. D: Appl. Phys. **52,** 353001 (2019).

[8] S. Büyükköse, B. Vratzov, J. van der Veen, P. V. Santos, and W. G. van der Wiel, Ultrahigh-frequency surface acoustic wave generation for acoustic charge transport in silicon, Appl. Phys. Lett. **102,** 013112 (2013).

[9] M. J. A. Schuetz, E. M. Kessler, G. Giedke, L. M. K. Vandersypen, M. D. Lukin, and J. I. Cirac, Universal Quantum Transducers Based on Surface Acoustic Waves, Phys. Rev. X **5,** 031031 (2015).

[10] P. V. Santos, M. E. Msall, and S. Ludwig, Acoustic field for the control of electronic excitations in semiconductor nanostructures, 2018 IEEE Int. Ultrason. Symp. (IUS), 1 (2018).

[11] T. Hesjedal, Surface acoustic wave-assisted scanning probe microscopy—a summary, Rep. Prog. Phys. **73,** 016102 (2009).

[12] J. H. Hoh and A. Engel, Friction effects on force measurements with an atomic force microscope, Langmuir **9,** 3310 (1993).

[13] L. D. Landau and E. M. Lifschitz, *Course of Theoretical Physics, Volume I, Mechanics* (Elsevier Ltd., Oxford, 1976).

[14] J. Tersoff, Modeling solid-state chemistry: Interatomic potentials for multicomponent systems, Phys. Rev. B **39,** 5566 (1989).